PHOTONICS Research

Dual-microcomb generation via a monochromatically pumped dual-mode microresonator

Runlin Miao,[1] Ke Yin,[2,3] Chao Zhou,[4] Chenxi Zhang,[3] Zhuopei Yu,[3] Xin Zheng,[1] and Tian Jiang[5,*] ⓘ

[1]*National Innovation Institute of Defense Technology, Academy of Military Sciences PLA China, Beijing 100071, China*
[2]*Beijing Institute for Advanced Study, National University of Defense Technology, Beijing 100000, China*
[3]*College of Advanced Interdisciplinary Studies, National University of Defense Technology, Changsha 410073, China*
[4]*College of Electronic Science and Technology, National University of Defense Technology, Changsha 410073, China*
[5]*Institute for Quantum Science and Technology, College of Science, National University of Defense Technology, Changsha 410073, China*
Corresponding author: tjiang@nudt.edu.cn

Microcombs have enabled a host of cutting-edge applications from metrology to communications that have garnered significant attention in the last decade. Nevertheless, due to the thermal instability of the microresonator, additional control devices like auxiliary lasers are indispensable for single-soliton generation in some scenarios. Specifically, the increased system complexity would be too overwhelming for dual-microcomb generation. Here, we put forward a novel approach to mitigate the thermal instability and generate the dual-microcomb using a compact system. This process is akin to mode-division multiplexing, as the dual-microcombs are generated by pumping the dual-mode of a single Si_3N_4 microresonator with a continuous-wave laser. Both numerical simulations and experimental measurements indicate that this innovative technique could offer a straightforward way to enlarge the soliton existence range, allowing entry into the multistability regime and triggering another microcomb alongside the main soliton pulse. This outcome not only shines new light on the interaction mechanism of microresonator modes but also provides an avenue for the development of dual-microcomb-based ranging and low phase noise microwave generation. © 2023 Chinese Laser Press

https://doi.org/10.1364/PRJ.507227

1. INTRODUCTION

The microresonator-based frequency comb (microcomb) [1,2], generated by pumping a continuous-wave (CW) laser into a high-Q optical microresonator, has gained significant attention in research due to its unparalleled miniaturization. As a type of coherent microcomb, the dissipative Kerr soliton [3] is as a self-reinforcing wave packet that maintains its shape while circulating around a microresonator. It has facilitated numerous applications in communications [4–6], laser ranging [7,8], optical clocks [9], microwave photonics [10–12], and photonic signal processing [13–15]. The dual-microcomb, consisting of two microcombs with slightly different repetition rates δf, could be utilized to coherently down-convert the signal microcomb to the radio-frequency (RF) by beating it with another soliton microcomb. The large optical spectrum down-conversion factor $f_r/\delta f$ eliminates the need for high-speed photodetectors. The dual-microcomb scheme has displayed exceptional potential in application scenarios of dual-comb spectroscopy [16,17], RF waveform synthesis [18], Vernier spectrometer [19,20], ranging [21,22], and broadband signal channelization [23,24].

Thermo-optic instability is currently a significant challenge for the generation of the soliton microcomb when the pump enters into the red-detuned regime of integrated optical microresonators. To address this concern, sophisticated techniques were developed to mitigate this effect, including auxiliary laser-assisted thermal compensation [25–31], single-sideband rapid frequency sweeping [32], pump modulation [33,34], and pulse-driven schemes [35,36]. However, excessive implementation of control devices adds complexity to the microcomb generation system. When it comes to dual-microcomb generation, either two sets of single-microcomb generation schemes [37], the use of a single laser to pump two independent microresonators [19,38], or the use of two lasers to pump a single microresonator [39,40], is always employed with a larger system volume.

Therefore, there are insistent demands for compact dual-microcomb generation schemes through only a monochromatically pumped single microresonator. Previous researches have explored dual-microcomb generation through opposite direction pumping [41], spatial mode multiplexing [42], and

polarization mode multiplexing [43–45]. However, opposite direction pumping still requires extra acousto-optic modulators (AOMs), and spatial mode multiplexing has only been demonstrated in crystalline resonators. Polarization mode multiplexing with adjacent dual-mode type stands out because multiple modes are widespread in integrated waveguides. Recent studies also prove that the dual-mode scheme could prolong the soliton existence range and simplify the setups [46,47]. Additionally, due to the Kerr nonlinear effect [48,49], the pump laser could enter the multistability regime where one mode overlaps with the second mode so that the dual-microcomb source with different repetition rates could also be realized.

In this work, a novel 50 GHz dual-microcomb generation scheme is proposed and experimentally demonstrated by pumping two adjacent modes in a microresonator with a single CW laser. This scheme could mitigate the photo-thermal effect and enlarge the soliton existence range from only 1.7 to 740 MHz. Furthermore, we not only realize stable generation of a TE_{00}-polarized soliton microcomb and a TE_{10}-polarized primary microcomb but also observe a TE_{00}-polarized soliton microcomb and a TE_{10}-polarized chaotic microcomb. Numerical simulation is also conducted to demonstrate the thermal compensation effect and the capacity for dual-microcomb generation. From an application perspective, the demonstrated dual-microcomb generation technology has the superiority in terms of miniaturization and ease of operation, and it would also pave the way for microwave signal generation and interference-free laser ranging applications.

2. MONOCHROMATICALLY PUMPED DUAL-MODE SCHEME

Figure 1(a) illustrates the concept that the dual-microcomb could be simultaneously generated by driving a single micro-resonator with a single CW laser field. The cavity transfer function for pumping is illustrated in the inset. Two nearby transverse electric modes (the fundamental TE_{00} mode and the first-order TE_{10} mode) with a small mode frequency spacing δ_ω could be synchronously triggered by the bistability of Kerr cavities. Specifically, by adjusting appropriate pump power and laser frequency sweep velocity parameters accordingly, both cavity resonance (C-resonance, CW component) and soliton resonance (S-resonance, soliton component) of TE_{10} mode could be overlapped with the S-resonance of TE_{00} mode. Therefore, along with the soliton microcomb of the TE_{00} mode, primary comb, secondary comb, chaotic comb, and soliton comb of TE_{10} mode could also be generated simultaneously when exceeding its modulational instability (MI) threshold, thus forming the desired dual-microcomb.
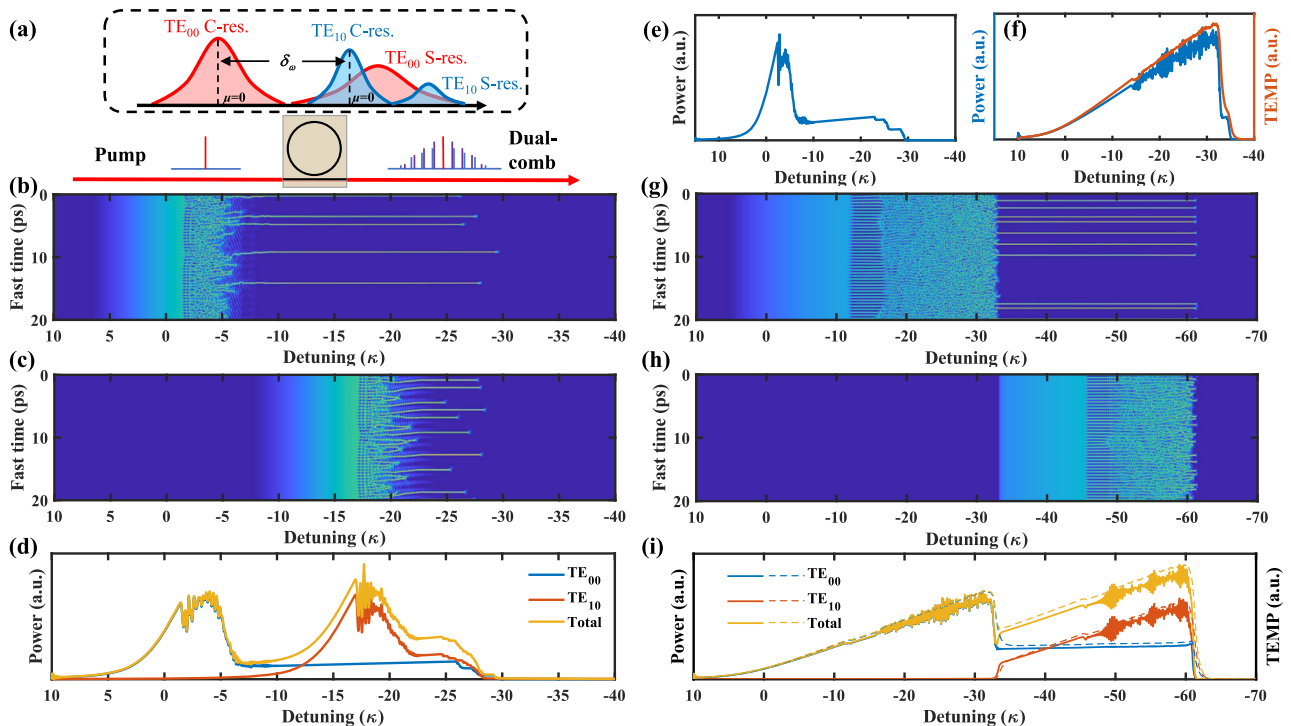
Fig. 1.   Principle and numerical simulations for dual-microcomb generation with the dual-mode scheme. (a) Theory illustration for dual-micro-comb generation with a single pump and two adjacent modes (TE_{00} mode and TE_{10} mode), in which the C-resonance (C-res.) corresponds to the CW component and the S-resonance (S-res.) corresponds to the soliton component. (b) and (c) are simulated intracavity field evolutions of TE_{00} mode and TE_{10} mode, respectively, without the photo-thermal effect. (d) Numerical simulation of the intracavity powers of TE_{00} mode, TE_{10} mode, and the total without the photo-thermal effect, showing the formation of dual-microcomb. (e), (f) Numerical simulations of the intracavity power evolutions (blue) of single-mode (e) without or (f) with the photo-thermal effect. (f) Temperature-induced resonance frequency variation is indicated by the red line. (g) and (h) are simulated intracavity field evolutions of TE_{00} mode and TE_{10} mode, respectively, with the photo-thermal effect. (i) Numerical simulations of the intracavity powers and temperature-induced resonance frequency variations of TE_{00} mode, TE_{10} mode, and the total with the photo-thermal effect. The simulations reveal the soliton step extension of TE_{00} mode utilizing the dual-mode scheme.

Since there are two modes being pumped, two modified Lugiato-Lefever equations (LLEs) are required to describe the dynamics evolution process of the dual-microcomb in TE_{00} mode and TE_{10} mode, respectively. It is also assumed that the dual-mode resonances could support their own sets of microcomb generation without interaction in the case of large group velocity difference. Moreover, the free spectral range (FSR) difference is out of consideration in the simulation. Additionally, by including a temperature variation in the detuning term, the overall dual-microcomb formation process can be comprehensively understood as below [50,51]:

$$\frac{\partial A_1}{\partial t} = \left(-\frac{\kappa_1}{2} + i(\omega_0 - \omega_p) + iD_{\omega 1} + iT \right)A_1 + ig_\omega |A_1|^2 A_1$$
$$+ \sqrt{\kappa_{ex1}} \cdot s_{in},$$

(1)

$$\frac{\partial A_2}{\partial t} = \left(-\frac{\kappa_2}{2} + i(\omega_0 - \omega_p) + i\delta_\omega + iD_{\omega 2} + iT \right)A_2$$
$$+ ig_\omega |A_2|^2 A_2 + \sqrt{\kappa_{ex2}} \cdot s_{in},$$

(2)

with

$$\frac{\partial T_1}{\partial t} = \left(\frac{\xi}{\tau} \right) \cdot \overline{|A_1|^2} - \frac{T_1}{\tau},$$

(3)

$$\frac{\partial T_2}{\partial t} = \left(\frac{\xi}{\tau} \right) \cdot \overline{|A_2|^2} - \frac{T_2}{\tau},$$

(4)

$$T = T_1 + T_2,$$

(5)

where A is the intracavity field's envelope, $\kappa = \kappa_0 + \kappa_{ex}$ is the total cavity decay rate (with κ_0 being the intrinsic loss rate and κ_{ex} being the external coupling rate), ω_0 and ω_p are the angular frequencies of the pumped TE_{00} cold resonance and the laser, respectively, D_ω is the microresonator dispersion, T is the thermal resonance shift, g_ω is the single photon-induced Kerr frequency shift, $s_{in} = P_{in}/\hbar\omega_0$ is the driving photon flux, δ_ω is the mode spacing between TE_{00} mode and TE_{10} mode, ξ is the thermal strength coefficient, and τ is the thermal relaxation time. The subscripts "1" and "2" for the aforementioned parameters correspond to the TE_{00} mode and TE_{10} mode, respectively. Referring to the subsequent experimental characterization results of the Si_3N_4 microresonator, the partial parameter values in the numerical simulations are as follows: $\kappa_1/2\pi = 50$ MHz, $\kappa_2/2\pi = 75$ MHz, $\kappa_{ex1}/2\pi = \kappa_{ex2}/2\pi = 25$ MHz, $D_{2(TE_{00})}/2\pi = 0.19$ MHz, $D_{2(TE_{10})}/2\pi = 0.26$ MHz, and $P_{in} = 250$ mW.

Initially, numerical simulation of dual-microcomb generation without the photo-thermal effect ($T = 0$, $\delta_\omega/2\pi = 750$ MHz) was conducted. Figures 1(b) and 1(c) exhibit the intracavity field evolutions for TE_{00} mode and TE_{10} mode, respectively, and Fig. 1(d) illustrates the intracavity power variations of TE_{00} mode, TE_{10} mode, and the total. It is evident that various Kerr parametric oscillations (primary comb, secondary comb, chaotic comb, and soliton comb) of TE_{10} mode coincidentally exist with the soliton state of TE_{00} mode.

However, owing to the photo-thermal effect, when the microcomb transforms from a high-power chaotic state to a low-power soliton state, the resonator would have a frequency blueshift with a fall of temperature, thus hindering the formation of soliton microcombs. Figures 1(e) and 1(f) showcase the simulation results of intracavity power evolution for single-mode pumping without or with the photo-thermal effect. The temperature-related parameters used are $\xi = 0.1368$ W^{-1} and $\tau = 10^{-8}$ s. The results suggest that the soliton existence range shrinks vastly from $21.5\,\kappa_1$ to $2\,\kappa_1$, posing a significant hurdle for soliton microcomb generation. Here, the soliton existence range refers to the frequency range that the pump laser can sweep without losing the soliton microcombs. Fortunately, the monochromatically pumped dual-mode scheme could overcome such thermal instability and diminish the thermal variation when forming solitons within the microresonator. Figures 1(g) and 1(h) show the simulated intracavity field evolutions of TE_{00} mode and TE_{10} mode, respectively, at $\delta_\omega/2\pi = 1000$ MHz. This mode spacing is carefully chosen in the simulation process to achieve the best thermal compensation result. Although the soliton step in TE_{10} mode is still extremely short or possibly even negligible, the soliton existence range in TE_{00} mode has been significantly increased from $2\,\kappa_1$ to $28\,\kappa_1$, which is even greater than that when occurring without the photo-thermal effect.

The reason could be elucidated from Fig. 1(i), which displays intracavity power and temperature-induced resonance frequency variations of TE_{00} mode, TE_{10} mode, and the total cavity. As the microcomb of TE_{00} evolves from the primary comb to the chaotic comb, the intracavity temperature increases gradually and reaches the peak lastly. Once the low-power soliton comb is initiated, the pump laser locates itself at the red side of the TE_{00} resonance frequency, simultaneously cooling the microresonator. Meanwhile, it also enters the blue-detuned and thermal self-lock region of the TE_{10} resonance frequency. By heating up the TE_{10} mode, the total cavity thermal change could be mitigated, thus making the soliton state of the TE_{00} mode more achievable. When the pump laser moves toward the longer wavelength, it could arouse the MI of TE_{10} mode, leading to a simultaneous increase of the total cavity temperature and a decrease of TE_{00} mode resonance frequency. The effective detuning between the pump laser and TE_{00} resonance frequency grows slower than the absolute frequency sweep range of the pump laser itself, which explains why the soliton existence range can be larger than that without photo-thermal effect. As a consequence, our theoretical analysis shows that the monochromatically pumped dual-mode scheme can not only alleviate the microcavity thermal variations and enlarge the soliton existence range but also establish the theoretical principles for dual-microcomb generation.

3. RESULTS AND DISCUSSION

A. Device Characterization and Soliton Step Extension

Figure 2(a) shows the schematic of compact experimental setups for dual-microcomb generation. The CW pump laser used is an external-cavity diode laser with its wavelength around 1550 nm, which can be tuned by a piezo actuated by a ramp
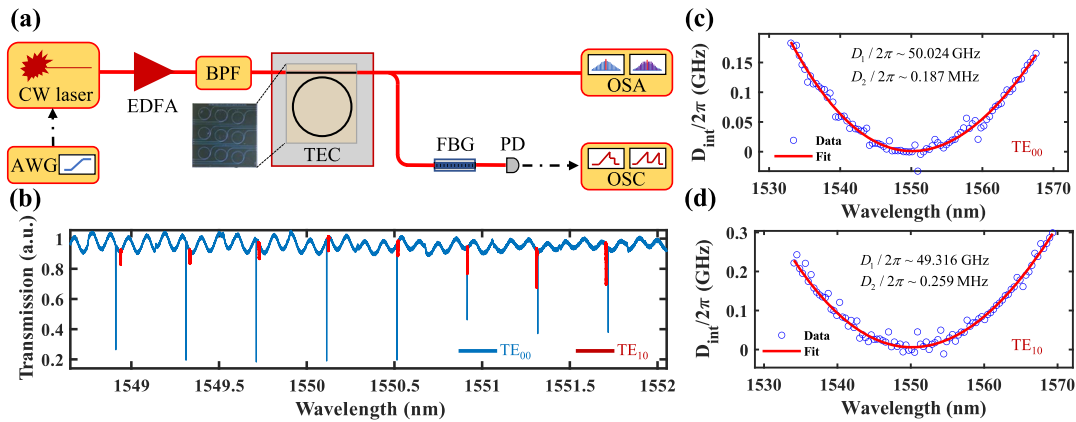
Fig. 2. Dual-microcomb generation experimental setups and characterization. (a) Schematic of the experimental setup. The inset shows a microscope image of one fabricated Si_3N_4 microresonator chip. AWG, arbitrary waveform generator; EDFA, erbium-doped fiber amplifier; BPF, bandpass filter; TEC, thermoelectric cooler; FBG, fiber Bragg grating; PD, photodetector; OSA, optical spectrum analyzer; OSC, oscilloscope. (b) Transmission spectrum of the microresonator used for dual-microcomb generation. The blue and red lines are measured data for TE_{00} and TE_{10} modes, respectively. (c) and (d) are experimentally measured dispersion profiles D_{int} of TE_{00} and TE_{10} modes, respectively. The blue circles are the measured data, and the red lines are the fitting curves.

voltage signal from an arbitrary waveform generator (AWG). Then, the CW laser is power amplified by an erbium-doped fiber amplifier (EDFA) and filtered by a band-pass filter (BPF) to reject amplified spontaneous emission (ASE) noise from the EDFA. The laser power is subsequently coupled into a silicon nitride (Si_3N_4) ring microresonator fabricated through a subtractive process [52,53]. The Si_3N_4 microresonator employed here has a radius of 456 µm and a cross section of 2.2 µm × 0.82 µm. The temperature of the microresonator chip is maintained at 28.50°C by a thermoelectric cooler (TEC). For the microcomb optical output, one part of the microcomb excluding the strong pump by a fiber-Bragg grating (FBG) is detected by a photodiode (PD), followed by an oscilloscope to monitor the power evolution process. The other part is monitored by an optical spectrum analyzer (OSA).

Experimentally, we selected the dual-mode in close proximity to each other near 1550 nm for pump by adjusting the polarization state. Figure 2(b) presents a characterization result of the sectional transmission spectrum, which exhibits two sets of TE polarization modes—the fundamental TE_{00} mode and the first-order TE_{10} mode. These modes can be easily distinguished based on the different FSRs. The significantly decreasing extinction ratio near 1550.91 nm indicates a weak mode coupling between the two modes. By extracting and fitting the measured TE_{00} and TE_{10} data [54], the integrated dispersion D_{int} was calculated and is plotted in Figs. 2(c) and 2(d), respectively. Their FSRs are extracted as 50.024 and 49.316 GHz, respectively, with a difference of ~0.708 GHz that determines the repetition rate difference of the dual-microcomb. Besides, their group velocity dispersion (GVD) $D_2/2\pi$ was also fitted to be 0.187 and 0.259 MHz, respectively, implying an anomalous GVD that is necessary for soliton generation. It is also mentioned that this dual-mode phenomenon is extensively present in the multimode waveguide with wide cross-section width. Due to the differences in FSR and dispersion, there will be two resonances belonging to different

modes that unavoidably cross each other, indicating that the design can be reproduced and fabricated with ease.

Selecting proper mode spacing between TE_{00} mode and TE_{10} mode is crucial for dual-microcomb generation. For overlarge mode spacing, the dual-microcomb will evolve in sequence, and the thermal compensation effect between the dual-mode will never occur. If the mode spacing is too close, only one microcomb can be aroused due to the overlapped transmission spectrum. Figure 3(a) shows the detailed transmission spectrum of the deliberately chosen TE_{00} and TE_{10} pumping modes centered around C34 (channel 34 of the C band, 1550.12 nm) so that the generated microcomb can be easily separated with a commercial wavelength-division demultiplexer. The resonance wavelengths of the two modes are 1550.1134 and 1550.1241 nm, respectively, with the resonance frequency of TE_{00} mode being approximately 1.34 GHz higher than that of the TE_{10} mode. Figures 3(b) and 3(c) show typical TE_{00} and TE_{10} resonance profiles. When a Lorentzian fit is used, it is found that the total cavity decay rates of TE_{00} and TE_{10} were $\kappa_1/2\pi = 46.4$ MHz and $\kappa_2/2\pi = 73.4$ MHz, indicating loaded Q values of 4.2×10^6 and 2.6×10^6, respectively.

As for microcomb generation, the wavelength of the pump laser and the output power of the EDFA are set to ~1550.12 nm and 1380 mW, respectively. The on-chip power P_{in} is calculated to be about 310 mW considering the 3 dB loss from the band-pass filter and the 3.4 dB loss from the fiber-chip coupling packaging. The microcomb can be excited by scanning the pump laser through the resonant mode from the blue-detuned to the red-detuned side. Here, a simple piezoelectric frequency sweep method [55] is employed with a velocity of ~91.4 MHz/ms. By adjusting the polarization state, when the pumped mode exclusively comprises the fundamental TE_{00} mode, the power evolution of the measured microcomb result is displayed in Fig. 3(c). Due to the thermally-induced resonance frequency shift in the cavity, the soliton state is incapable
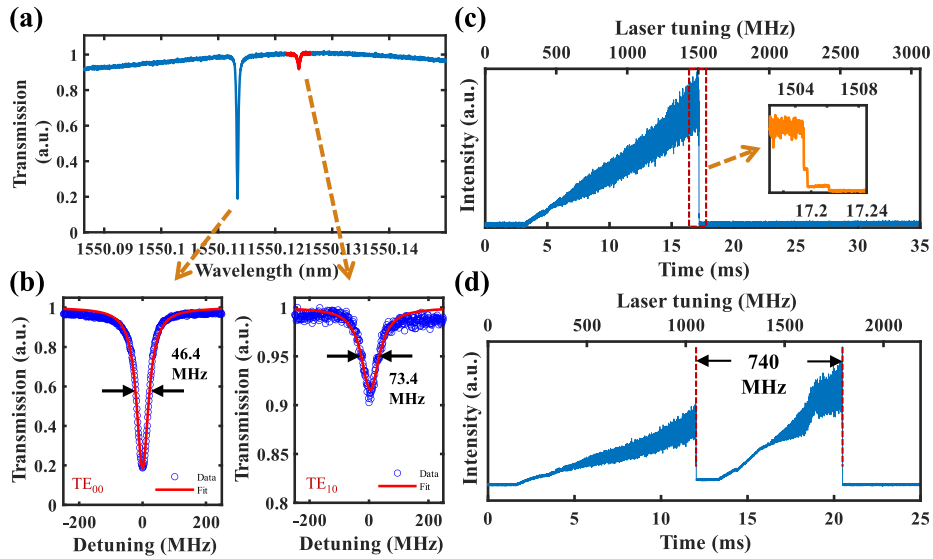
Fig. 3. Soliton existence range extension through pumping dual adjacent modes. (a) Measured transmission spectrum of TE_{00} and TE_{10} modes for the pump near 1550.12 nm. (b) Microresonator loss results of TE_{00} mode (left) and TE_{10} mode (right), respectively. The blue dots and red lines are the measured results and Lorentzian fits. (c) and (d) are observed soliton steps versus scan time or laser tuning frequency for pumping single-mode and dual-mode, respectively. The inset in (c) is the enlarged soliton step. The soliton existence range is increased obviously from (c) 1.7 MHz to (d) 740 MHz. The frequency-coordinate of (c) and (d) was calibrated by a fiber ring with an FSR of ∼33 MHz.

of existence due to the short soliton step (1.7 MHz), which is consistent with the numerical simulation shown in Fig. 1(f). For the result of the dual-mode scheme presented in Fig. 3(d), the intracavity power evolution reveals two triangular profiles. One represents the Kerr parametric oscillation from the TE_{00} mode, while the other corresponds to the TE_{10} mode. Moreover, the single-soliton step of the TE_{00} mode coincides with the parametric oscillation microcomb of the TE_{10} mode, resulting in a total length of ∼740 MHz, which is 435 times greater than that of the single-mode approach. As illustrated in Figs. 1(g)–1(i), the TE_{10} mode can mitigate the thermally-induced resonance frequency shift caused by intracavity power change, therefore extending the soliton existence range.

Apart from piezoelectric frequency sweep for soliton microcomb generation, the monochromatically pumped dual-mode scheme could also effectively reduce the thermal variation of the microresonator similar to the auxiliary laser-assisted thermal compensation scheme [25]. The soliton state can be easily reached even by slow temperature control to tune the pump laser wavelength or change the mode resonance frequency according to the photo-thermal effect. As depicted in Fig. 4, here we chose to slowly adjust the temperature of the microcavity chip via a TEC to excite single-soliton microcomb generation. The pump laser is first set to the blue-detuned side of the TE_{00} mode. Then, decreasing the chip temperature from 28.52°C to 28.08°C within 70 s (forward frequency tuning), a multiple-soliton step could be easily accessed as illustrated in Fig. 4(a). Based on the relationship between the chip temperature and the resonance wavelength $d\lambda/dT$ of ∼0.0227 nm/K [38], the relative frequency sweep velocity is determined to be about 17.8 MHz/s, which is over 5000 times slower than that of the piezoelectric frequency sweep. This illustrates that the Kerr microresonator with a dual-mode scheme is thermally in-
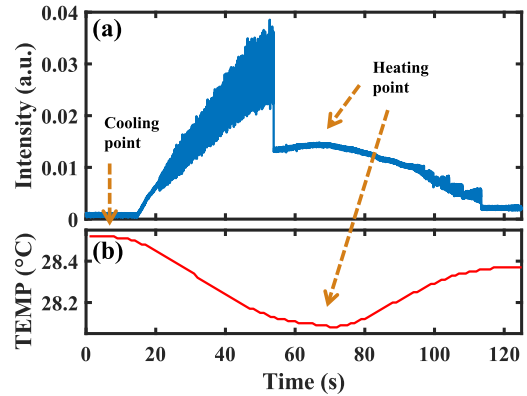
Fig. 4. Single-soliton microcomb generation through slow temperature tuning. (a) Microcomb power trace and (b) chip temperature variation under cooling and heating conditions, respectively. The discrete steps suggest different soliton states.

sensitive and the pump laser frequency within the red-detuned side is also allowed. It reveals that the tunable pump laser with relatively high noise could be replaced by an ultra-narrow linewidth laser to improve the coherence of microcomb.

As noted in Ref. [50], a backward frequency tuning strategy could be employed to deterministically achieve the single-soliton state due to the thermal nonlinearity of the Kerr microresonator and the non-degenerate lower boundaries of soliton existence ranges with respect to different soliton numbers. Here, backward frequency tuning is realized by heating the chip from 28.08°C to 28.37°C temperature within 47 s. Therefore, the staircase patterned microcomb power trace can be seen from Fig. 4(a), and each soliton step corresponds

to a specific soliton state. The lowest power step is on behalf of the single-soliton state and could be kept stable.

B. Dual-Microcomb Generation and RF Beat Note Analysis

Back to the piezoelectric frequency sweep method, several experimental tests for microcomb generation were conducted by repeatedly scanning the pump laser over the dual-mode region at $P_{in} = 310$ mW. Five representative intracavity power results are recorded in Fig. 5(a), which is consistent with the numerical simulation results presented in Figs. 1(g)–1(i). Besides the single-soliton that was already shown in Fig. 3(d), zero-soliton and multiple-solitons with $N = 2$ to 4 are also obtained, according to the linear relation between soliton numbers and the detected microcomb power voltage at position ①, where only a single microcomb exists. Figure 5(c) shows the single-soliton microcomb spectrum of a 50 GHz mode spacing measured with an OSA, which is well fitted by the sech^2 function. The spectrum's 3 dB bandwidth is roughly 29.47 nm, corresponding to a Fourier-transform-limited pulse duration of 85 fs. The spectrum of the two-soliton state shown in Fig. 5(d) indicates a soliton separation of ∼30°, retrieved via inverse Fourier transform of the optical spectrum. Furthermore, Figs. 5(e) and 5(f) are the corresponding spectra for $N = 3$ and 4, respectively.

Figure 5(g) records the statistical results of soliton numbers with 30 repeated experimental scanning processes at three different on-chip pump power levels. At $P_{in} = 310$ mW, though the success rate for soliton microcomb generation is only 40%, the majority of the microcombs are the two-soliton microcomb and single-soliton microcomb, making them suitable for microwave photonics and other applications. As for $P_{in} = 325$ and 380 mW, both success rates can reach 100%. Specifically, soliton numbers are distributed from $N = 1$ to 6 with on-chip power of 325 mW, whereas multiple-solitons are mainly found from $N = 4$ to 7 at $P_{in} = 380$ mW. As the pump laser power increases, the success rate for soliton microcomb generation and the soliton numbers would improve as well. The reason can be that the increase in pump laser power could cause more thermally-induced red-shift of the resonance frequency, leading to a decrease in the frequency interval between the triangular profile peak of TE_{00} mode and the resonant frequency mode of TE_{10}. At this point, the TE_{10} mode could further help alleviate the thermal change within the cavity, and the pump laser is more likely to stay at the closer red-shift side of TE_{00} mode resonance, thus leading to multiple-soliton microcomb generation and achieving a higher excitation success rate.

When tuning the pump laser to positions ②, ③, and ④ within the second triangular profile of the intracavity power, the dual-microcomb could appear in different states. As can be seen from Figs. 6(a)–6(c), the dual-microcomb evolves from a single-soliton, primary comb (②) to a single-soliton, secondary comb (③), and eventually to a single-soliton, chaotic comb (④). Moreover, the dual-microcomb could remain stable for at least 2 h without any active feedback technique, which meets the majority of application requirements. It also demonstrates that the chaotic state of the TE_{10} mode with high and unstable energy does not affect the soliton state of the TE_{00} mode. Due to the thermal instability, the second microcomb generated from the Kerr parametric oscillation of TE_{10} mode failed to reach soliton state in the experiment. The illustration in Fig. 5(b) shows that, when considering the microcavity thermal effect, S-resonance of the TE_{00} mode is solely covered with the
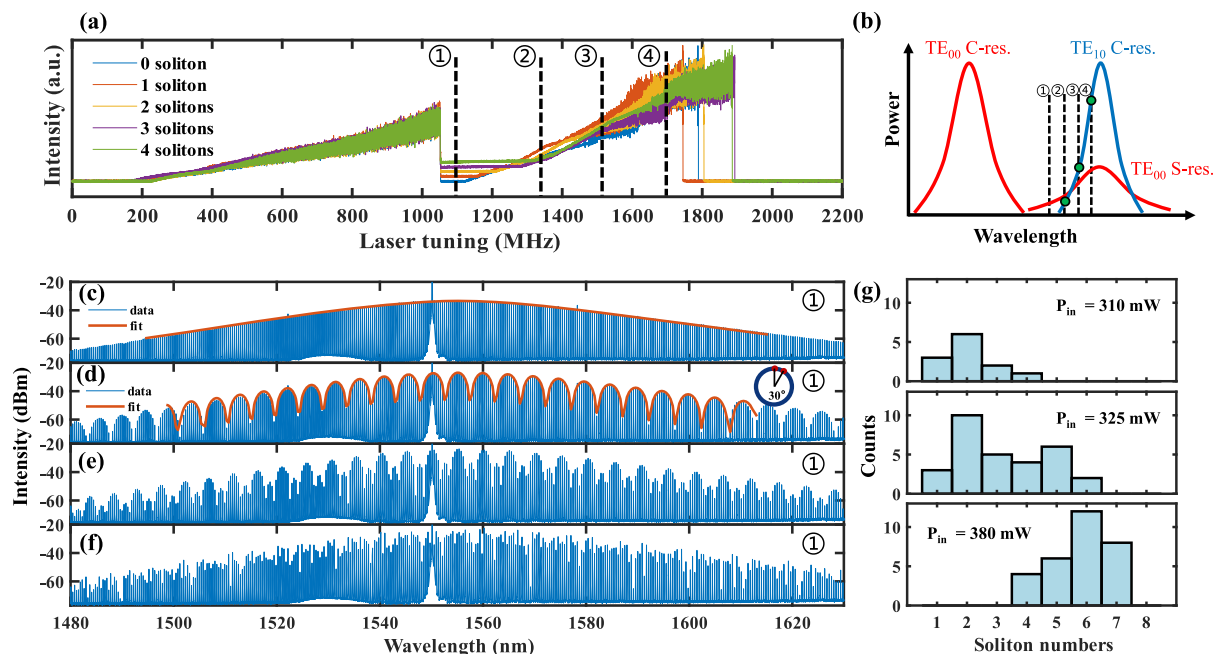
Fig. 5. Experimental soliton results. (a) Collected powers of microcombs for $N = 0$-, 1-, 2-, 3-, 4-soliton states of 50 GHz mode spacing at $P_{in} = 310$ mW. ①, ②, ③, ④ represent different frequency positions for dual-microcomb generation. (b) Principle of the dual-microcomb generation when considering the microcavity thermal effect. (c)–(f) Optical spectra for $N = 1$-, 2-, 3-, 4-soliton states at ① position. The red lines show a fitted sech^2 envelope (single-soliton) and a fitted 2-soliton envelope type, respectively. The inset of (d) shows the relative soliton position. (g) Statistics of soliton numbers with 30 repeated microcomb excitation processes at $P_{in} = 310$ mW, 325 mW, and 380 mW, respectively.
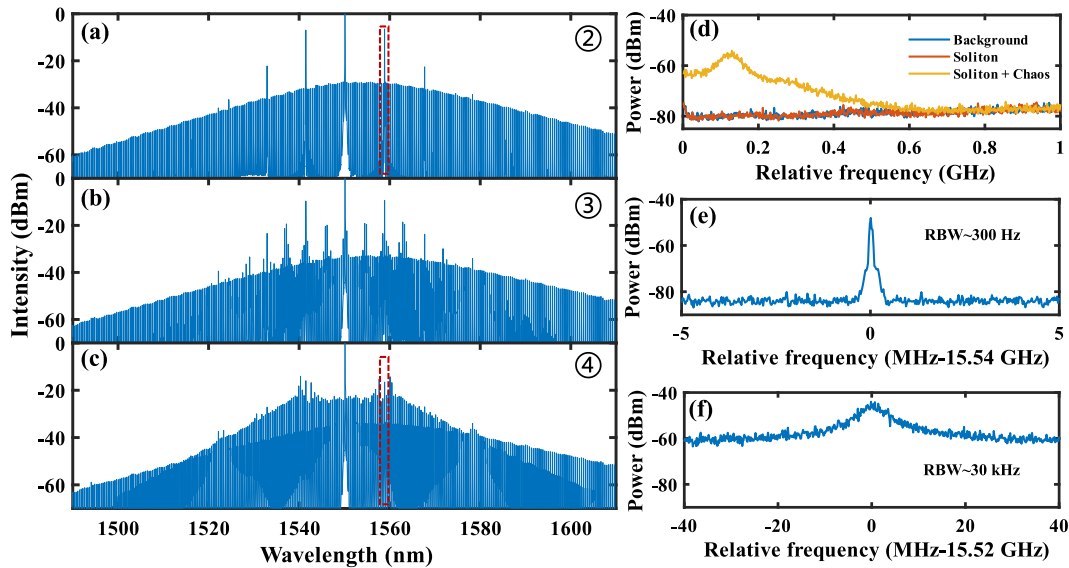
Fig. 6. Dual-microcomb spectra and RF beat notes. (a)–(c) Different dual-microcomb optical spectra at ② (single-soliton and primary comb), ③ (single-soliton and secondary comb), and ④ (single-soliton and chaotic comb) positions, respectively. (d) RF noise spectra of the soliton and dual-microcomb. The photodiode noise floor is overlapped by that of the single soliton. (e) and (f) are corresponding 15.5 GHz heterodyne beat notes of the two adjacent lines of the dual-microcomb at ② and ④ positions, respectively.

C-resonance of the TE_{10} mode, while the S-resonance of the TE_{10} mode cannot be reached.

Figure 6(d) plots the RF noise spectra of various microcombs, which were measured through an electrical spectrum analyser (ESA) by detecting the microcombs excluding the pump line. As for single-soliton or single-soliton, primary comb, the RF noise levels are equal to the background noise levels, showcasing the high coherence of microcombs. However, the yellow line in the RF noise spectra highlights the chaotic nature of the single-soliton, chaotic comb dual-microcomb. Moreover, microwave signals can be extracted from the dual-microcomb by heterodyning a pair of comb teeth with a tunable BPF (~0.5 nm bandwidth). As shown in Fig. 6(a), the first tooth of the primary comb and the 22nd tooth of the single-soliton microcomb are filtered and detected by the high-speed detector. An RF amplifier with ~27 dB signal gain is employed for signal amplification, although the combs used for beating are far from the pump laser, which may deteriorate the linewidth result to some extent. Figure 6(e) shows the collected 15.54 GHz signal with 3 dB bandwidth of ~39.5 kHz with a resolution bandwidth (RBW) of 300 Hz. It proves that the single-soliton and primary comb still has a high coherence with each other. Further, all-optical locking could be considered to improve the mutual coherence. The FSR difference between TE_{00} and TE_{10} modes can be deduced as ~0.706 GHz, which is similar to that of characterization. Moreover, due to the Vernier effect, the second and even more lines of the primary comb could also beat up with the single-soliton to generate different coherent microwave signals such as ~6.08 GHz (44 × 0.706 GHz – 25 GHz = 6.08 GHz) + N × 25 GHz and ~3.38 GHz(50 GHz – 66 × 0.706 GHz = 3.38 GHz)+ N × 25 GHz (for $N = 0, 1, 2…$).

For the single-soliton & chaotic comb, Fig. 6(f) shows the heterodyne beat note result at the same filtered region, which

has a wider 3 dB bandwidth of ~5.3 MHz on a high noise floor. The chaotic comb has been recently applied in various applications such as interference-free LiDAR [22,56,57], optical chaos communication [58], and random number generation [59] depending on its optical spatiotemporal chaos characterization. Compared to the chaotic comb, the single-soliton here could be regarded as a local oscillator light to realize parallel down-conversion for different pairs of the dual-microcomb teeth. For the dual-microcomb, both in the soliton state, which could be used in the dual-comb spectroscopy if assisted by the method of pump modulation, or adopting microresonators with higher Q in the future, it could also be achieved. In addition, it needs to be mentioned that the conversion efficiency is improved from 0.45% (single-soliton microcomb) to 9.58% (single-soliton and chaotic comb), which illustrates that the dual-microcomb generation with a monochromatically pumped dual-mode microresonator could make the utmost of the pump laser energy.

4. CONCLUSION

In conclusion, we have demonstrated a novel approach to access the 50 GHz dual-microcomb generation via a monochromatically pumped dual-mode microresonator. This scheme has considerable potential toward miniaturization and integration, and it is applicative for other material platforms as well. Both numerical simulations and experimental measurements were conducted to comprehend the mechanisms and forming processes for the dual-microcomb. By taking advantage of the thermal compensation effect from the TE_{10} mode, the soliton existence range of TE_{00} mode could be increased from 1.7 to 740 MHz. It simplifies the soliton excitation procedure with either piezoelectric frequency sweeping or slow temperature control. Besides, dual-microcombs of the mutual-coherent

soliton, primary microcomb and incoherent soliton, chaotic microcomb are verified with both spectral analysis and RF beat note measurements. For further practical applications, the dual-microcomb with different polarization modes (TE_{00} and TE_{10}) could be separated by the compact inversely-designed silicon photonics device [60]. Furthermore, the methods presented in this study could serve as motivation for studying the interaction mechanism of microresonator modes in Kerr microcomb generation.

Disclosures. The authors declare no conflicts of interest.

Data Availability. Data underlying the results presented in this paper are not publicly available at this time but may be obtained from the authors upon reasonable request.

REFERENCES

1. P. Del'Haye, A. Schliesser, and O. Arcizet, *et al.*, "Optical frequency comb generation from a monolithic microresonator," Nature **450**, 1214–1217 (2007).
2. W. Wang, L. Wang, and W. Zhang, "Advances in soliton microcomb generation," Adv. Photonics **2**, 034001 (2020).
3. T. Herr, V. Brasch, and J. D. Jost, *et al.*, "Temporal solitons in optical microresonators," Nat. Photonics **8**, 145–152 (2013).
4. P. Marin-Palomo, J. N. Kemal, and M. Karpov, *et al.*, "Microresonator-based solitons for massively parallel coherent optical communications," Nature **546**, 274–279 (2017).
5. Y. Geng, H. Zhou, and X. Han, *et al.*, "Coherent optical communications using coherence-cloned Kerr soliton microcombs," Nat. Commun. **13**, 1070 (2022).
6. W. Shao, Y. Wang, and S. Jia, *et al.*, "Terabit FSO communication based on a soliton microcomb," Photonics Res. **10**, 2802–2808 (2022).
7. M. Yang, G. Wang, and Z. Wang, *et al.*, "Micrometer-precision absolute distance measurement with a repetition-rate-locked soliton microcomb," Opt. Lett. **48**, 4356–4359 (2023).
8. J. Wang, Z. Lu, and W. Wang, *et al.*, "Long-distance ranging with high precision using a soliton microcomb," Photonics Res. **8**, 1964–1972 (2020).
9. Z. L. Newman, V. Maurice, and T. Drake, *et al.*, "Architecture for the photonic integration of an optical atomic clock," Optica **6**, 680–685 (2019).
10. J. Liu, E. Lucas, and A. S. Raja, *et al.*, "Photonic microwave generation in the X- and K-band using integrated soliton microcombs," Nat. Photonics **14**, 486–491 (2020).
11. J. Hu, J. He, and J. Liu, *et al.*, "Reconfigurable radiofrequency filters based on versatile soliton microcombs," Nat. Commun. **11**, 4377 (2020).
12. B. Wang, J. S. Morgan, and K. Sun, *et al.*, "Towards high-power, high-coherence, integrated photonic mmWave platform with microcavity solitons," Light Sci. Appl. **10**, 4 (2021).
13. X. Xu, M. Tan, and B. Corcoran, *et al.*, "11 TOPS photonic convolutional accelerator for optical neural networks," Nature **589**, 44–51 (2021).
14. B. Bai, Q. Yang, and H. Shu, *et al.*, "Microcomb-based integrated photonic processing unit," Nat. Commun. **14**, 66 (2023).

15. H. Shu, L. Chang, and Y. Tao, *et al.*, "Microcomb-driven silicon photonic systems," Nature **605**, 457–463 (2022).
16. N. Picqué and T. W. Hänsch, "Frequency comb spectroscopy," Nat. Photonics **13**, 146–157 (2019).
17. Y. Wang, Z. Wang, and X. Wang, *et al.*, "Scanning dual-microcomb spectroscopy," Sci. China Phys. Mech. Astron. **65**, 294211 (2022).
18. B. Wang, Z. Yang, and S. Sun, *et al.*, "Radio-frequency line-by-line Fourier synthesis based on optical soliton microcombs," Photonics Res. **10**, 932–938 (2022).
19. B. Wang, Z. Yang, and X. Zhang, *et al.*, "Vernier frequency division with dual-microresonator solitons," Nat. Commun. **11**, 3975 (2020).
20. Q. Yang, B. Shen, and H. Wang, *et al.*, "Vernier spectrometer using counterpropagating soliton microcombs," Science **363**, 965–968 (2019).
21. J. Riemensberger, A. Lukashchuk, and M. Karpov, *et al.*, "Massively parallel coherent laser ranging using a soliton microcomb," Nature **581**, 164–170 (2020).
22. A. Lukashchuk, J. Riemensberger, and A. Tusnin, *et al.*, "Chaotic microcomb-based parallel ranging," Nat. Photonics **17**, 814–821 (2023).
23. F. Yin, Z. Yin, and X. Xie, *et al.*, "Broadband radio-frequency signal synthesis by photonic-assisted channelization," Opt. Express **29**, 17839–17848 (2021).
24. N. P. O'Malley, K. A. McKinzie, and M. S. Alshaykh, *et al.*, "Architecture for integrated RF photonic downconversion of electronic signals," Opt. Lett. **48**, 159–162 (2023).
25. H. Zhou, Y. Geng, and W. Cui, *et al.*, "Soliton bursts and deterministic dissipative Kerr soliton generation in auxiliary-assisted microcavities," Light Sci. Appl. **8**, 50 (2019).
26. R. Niu, M. Li, and S. Wan, *et al.*, "kHz-precision wavemeter based on reconfigurable microsoliton," Nat. Commun. **14**, 169 (2023).
27. C. Wang, J. Li, and A. Yi, *et al.*, "Soliton formation and spectral translation into visible on CMOS-compatible 4H-silicon-carbide-on-insulator platform," Light Sci. Appl. **11**, 341 (2022).
28. Y. Zhao, L. Chen, and C. Zhang, *et al.*, "Soliton burst and bi-directional switching in the platform with positive thermal-refractive coefficient using an auxiliary laser," Laser Photonics Rev. **15**, 2100264 (2021).
29. J. Gu, X. Li, and K. Qi, *et al.*, "Octave-spanning soliton microcomb in silica microdisk resonators," Opt. Lett. **48**, 1100–1103 (2023).
30. Q. Zhang, B. Liu, and Q. Wen, *et al.*, "Low-noise amplification of dissipative Kerr soliton microcomb lines via optical injection locking lasers," Chin. Opt. Lett. **19**, 121401 (2021).
31. Y. Wang, W. Wang, and Z. Lu, *et al.*, "Hyperbolic resonant radiation of concomitant microcombs induced by cross-phase modulation," Photonics Res. **11**, 1075–1084 (2023).
32. J. R. Stone, T. C. Briles, and T. E. Drake, *et al.*, "Thermal and nonlinear dissipative-soliton dynamics in kerr-microresonator frequency combs," Phys. Rev. Lett. **121**, 063902 (2018).
33. R. Miao, C. Zhang, and X. Zheng, *et al.*, "Repetition rate locked single-soliton microcomb generation via rapid frequency sweep and sideband thermal compensation," Photonics Res. **10**, 1859–1867 (2022).
34. T. Wildi, V. Brasch, and J. Liu, *et al.*, "Thermally stable access to microresonator solitons via slow pump modulation," Opt. Lett. **44**, 4447–4450 (2019).
35. E. Obrzud, S. Lecomte, and T. Herr, "Temporal solitons in microresonators driven by optical pulses," Nat. Photonics **11**, 600–607 (2017).
36. Z. Xiao, T. Li, and M. Cai, *et al.*, "Near-zero-dispersion soliton and broadband modulational instability Kerr microcombs in anomalous dispersion," Light Sci. Appl. **12**, 33 (2023).
37. N. G. Pavlov, G. Lihachev, and S. Koptyaev, *et al.*, "Soliton dual frequency combs in crystalline microresonators," Opt. Lett. **42**, 514–517 (2017).
38. R. Miao, K. Yin, and C. Zhang, *et al.*, "Stable soliton dual-microcomb generation via sideband thermal compensation for spectroscopy," Front. Phys. **10**, 989047 (2022).
39. W. Weng, R. Bouchand, and T. J. Kippenberg, "Formation and collision of multistability-enabled composite dissipative Kerr solitons," Phys. Rev. X **10**, 021017 (2020).
40. S. Zhang, J. M. Silver, and T. Bi, *et al.*, "Spectral extension and synchronization of microcombs in a single microresonator," Nat. Commun. **11**, 6384 (2020).

41. Q. Yang, X. Yi, and K. Y. Yang, *et al.*, "Counter-propagating solitons in microresonators," Nat. Photonics **11**, 560–564 (2017).

42. X. Xue, P. Grelu, and B. Yang, *et al.*, "Dispersion-less Kerr solitons in spectrally confined optical cavities," Light Sci. Appl. **12**, 19 (2023).

43. Y. Geng, Y. Xiao, and X. Han, *et al.*, "Polarization multiplexed dissipative Kerr solitons in an on-chip micro-resonator," Opt. Lett. **47**, 3644–3647 (2022).

44. H. Weng, A. Afridi, and M. McDermott, *et al.*, "Dual-microcombs generation with a single-pumped Si3N4 microresonator for tunable microwave oscillation," in *CLEO: Applications and Technology* (Optica Publishing Group, 2023), paper JTu2A.89.

45. G. Lin and T. Sun, "Mode crossing induced soliton frequency comb generation in high-Q yttria-stabilized zirconia crystalline optical microresonators," Photonics Res. **10**, 731–739 (2022).

46. H. Weng, A. A. Afridi, and J. Li, *et al.*, "Dual-mode microresonators as straightforward access to octave-spanning dissipative Kerr solitons," APL Photonics **7**, 066103 (2022).

47. H. Weng, J. Liu, and A. A. Afridi, *et al.*, "Directly accessing octave-spanning dissipative Kerr soliton frequency combs in an AlN microresonator," Photonics Res. **9**, 1351–1357 (2021).

48. Z. Wu, Y. Gao, and T. Zhang, *et al.*, "Coexistence of multiple microcombs in monochromatically pumped Si_3N_4 microresonators," Opt. Lett. **47**, 1190–1193 (2022).

49. W. Weng, R. Bouchand, and E. Lucas, *et al.*, "Heteronuclear soliton molecules in optical microresonators," Nat. Commun. **11**, 2402 (2020).

50. H. Guo, M. Karpov, and E. Lucas, *et al.*, "Universal dynamics and deterministic switching of dissipative Kerr solitons in optical microresonators," Nat. Phys. **13**, 94–102 (2016).

51. K. Liu, Z. Wang, and S. Yao, *et al.*, "Mitigating fast thermal instability by engineered laser sweep in AlN soliton microcomb generation," Photonics Res. **11**, A10–A18 (2023).

52. Z. Ye, H. Jia, and Z. Huang, *et al.*, "Foundry manufacturing of tight-confinement, dispersion-engineered, ultralow-loss silicon nitride photonic integrated circuits," Photonics Res. **11**, 558–568 (2023).

53. S. Wan, R. Niu, and J. Peng, *et al.*, "Fabrication of the high-Q Si_3N_4 microresonators for soliton microcombs," Chin. Opt. Lett. **20**, 032201 (2022).

54. Y. Luo, B. Shi, and W. Sun, *et al.*, "A vector spectrum analyzer of 55.1 THz spectral bandwidth and 99 kHz frequency resolution," arXiv, arXiv:2304.04295 (2023).

55. S. Wan, R. Niu, and Z. Wang, *et al.*, "Frequency stabilization and tuning of breathing solitons in Si_3N_4 microresonators," Photonics Res. **8**, 1342–1349 (2020).

56. R. Chen, H. Shu, and B. Shen, *et al.*, "Breaking the temporal and frequency congestion of LiDAR by parallel chaos," Nat. Photonics **17**, 306–314 (2023).

57. A. Lukashchuk, J. Riemensberger, and A. Stroganov, *et al.*, "Chaotic microcomb inertia-free parallel ranging," APL Photonics **8**, 056102 (2023).

58. L. Wang, X. Mao, and A. Wang, *et al.*, "Scheme of coherent optical chaos communication," Opt. Lett. **45**, 4762–4765 (2020).

59. B. Shen, H. Shu, and W. Xie, *et al.*, "Harnessing microcomb-based parallel chaos for random number generation and optical decision making," Nat. Commun. **14**, 4590 (2023).

60. A. Y. Piggott, E. Y. Ma, and L. Su, *et al.*, "Inverse-designed photonics for semiconductor foundries," ACS Photonics **7**, 569–575 (2020).